

Development of a Novel Adaptive Lead-Free Solder Containing Reinforcements Displaying the Shape-Memory Effect

I. DUTTA,^{1,3} B.S. MAJUMDAR,² D. PAN,¹ W.S. HORTON,¹ W. WRIGHT,¹ and Z.X. WANG²

1.—Center for Materials Science and Engineering, Department of Mechanical Engineering, Naval Postgraduate School, Monterey, CA 93943. 2.—Department of Materials Science and Engineering, New Mexico Institute of Mining and Technology, Socorro, NM 87801. 3.—E-mail: idutta@nps.navy.mil

Microelectronic solder joints are typically exposed to aggressive thermomechanical cycling (TMC) conditions during service. During TMC, strain localization occurs near solder/bond pad interfaces, where large, inelastic-shear strains accumulate, eventually causing low-cycle fatigue (LCF) failure of the joint. In this study, a novel methodology to mitigate the effects of strain localization within the joint is discussed, wherein the solder alloy is reinforced with a martensitic NiTi-based, shape-memory alloy (SMA). In this scheme, the SMA reinforcement deforms in shear concurrently with the solder during TMC and, subsequently, undergoes martensite-to-austenite ($M \rightarrow A$) transformation, placing the solder matrix next to the reinforcements in reverse shear. This is purported to reduce inelastic-strain localization within the solder and, thus, enhance joint life. In this paper, we present results of thermal-mechanical loading experiments conducted on a monolithic 95.5Sn-3.8Ag-0.7Cu solder, a Cu/Cu₆Sn₅ particle-reinforced solder, and NiTi-solder, single-fiber composites (SFCs) to elucidate the impact of the shape-memory effect on the overall joint behavior. It is demonstrated that during TMC, the phase transformations occurring in NiTi can significantly reduce the inelastic-strain range to which a joint is subjected (by ~25% in the present experiments). Finally, we report on the successful fabrication of a composite solder paste from which adaptive solders with a uniform distribution of about 5 vol.% of NiTi particulates may be produced.

Key words: Adaptive solder, composite, shape-memory alloys, shape-memory effect

INTRODUCTION

In flip-chip (FC) and ball-grid array (BGA) electronic packages, arrays of solder balls provide electrical and mechanical connections between a semiconductor chip and a polymeric circuit board. Because of the coefficient of thermal expansion (CTE) mismatch between semiconductor and polymer, solder joints are subjected to severe shear conditions during thermal cycling, leading to the accumulation of large inelastic strains within localized regions within joints.^{1–4} This accrual of inelastic strains leads

to low-cycle fatigue (LCF) of the solder joints, potentially resulting in joint failure and, hence, destruction of the package.⁵ As solder joints shrink progressively and the maximum, chip operating temperature increases with each advancing semiconductor technology node, the joints will be subjected to increasingly aggressive thermomechanical conditions by way of larger imposed shear strains and greater temperatures. This necessitates the development of innovative approaches to reduce inelastic-strain localization within solder joints to enhance joint life.

One way by which mitigation of internal strain localization has been attempted in recent years is by reinforcing the solder with small volume fractions of

(Received October 25, 2003; accepted December 17, 2003)

a stiff material to form a composite, resulting in increases in strength and creep and fatigue resistance.^{6–14} In-situ Ni_3Sn_4 and Cu_6Sn_5 dispersions in the solder have been observed to enhance stress-controlled fatigue life, although strain-controlled fatigue life appears to decrease because of increased void nucleation.⁶ Studies on solders reinforced by Ni, Ni-coated graphite particles, Cu, Cu-Sn intermetallics (Cu_3Sn and Cu_6Sn_5), $\text{FeSn}/\text{FeSn}_2$, and Ni_3Sn_4 ^{7,8,13} have shown improvements in strength relative to the monolithic solder and have enhanced the creep/fatigue life, particularly at slow strain rates.^{8,9} In addition, reinforcing the solder by small, stiff and hard particles reduces inelastic-strain localization within joints, thereby allowing more homogeneous deformation of the joint.¹⁴ However, the presence of reinforcements may also cause more rapid creep-damage accumulation, as reflected in the reduced performance under strain-controlled fatigue conditions,⁶ which are commonly encountered in microelectronics. Furthermore, because of its greater strength and stiffness, composite solders may subject the brittle semiconductor device to larger stresses, which is generally undesirable.

In response to these shortcomings of “passive” reinforcements, there has been considerable recent interest in developing “smart” or “adaptive” solder alloys reinforced by NiTi shape-memory alloy (SMA) particles.^{15–20} In particular, attempts have been made to fabricate NiTi particulate-containing solder alloys with the objective of exploiting the superelastic properties of austenitic NiTi (i.e., its ability to sustain large recoverable strains) to reduce the stresses in the solder matrix immediately adjacent to the reinforcements. To date, most of the effort has been focused on processing issues related to incorporating NiTi reinforcements in the solder, which is very difficult because of the poor wetting between NiTi and solder. Electroless Ni and Cu coatings on NiTi wires and particulates have been used to promote wetting of NiTi by the solder,^{16,17,19} although it has been noted that the wetting characteristics deteriorate with time and temperature exposure to the solder melt because of dissolution of the coating.¹⁷ This suggests that the coating approach may not be suitable for microelectronic applications, where multiple reflows are common. Furthermore, even when the NiTi particles are coated, obtaining a uniform distribution of NiTi in the solder has proved to be difficult.^{18,20} Indeed, to date, no published microstructure of solder with an even distribution of NiTi particulates can be found in the literature.

Furthermore, very limited mechanical-property data on NiTi-solder composites have been reported to date. Reinforcement by austenitic NiTi has been found to simultaneously enhance stiffness and ductility of the solder.⁴ This has been loosely ascribed to the inhibition of damage initiation in the solder caused by the large strains absorbed by the superelastic NiTi, although a clear mechanistic rationale is yet to emerge.⁴

Because austenitic NiTi is much stiffer and stronger than the solder,* it is unclear whether the load level necessary for the austenite-to-martensite ($A \rightarrow M$) transformation for superelasticity in NiTi can be reached in a solder matrix. Furthermore, because superelasticity typically occurs over a relatively small temperature range beyond the austenite finish temperature (A_f), it is unlikely that this phenomenon can be exploited over a significant part of TMC conditions, which typically span more than 100°C in typical microelectronic applications.

Because martensitic NiTi and solder have similar modulus and flow stress (E and σ_f) values,** it may be advantageous to use the one-way, shape-memory effect in martensitic NiTi reinforcements to produce adaptive lead-free solder joints, as this would enable simultaneous deformation of the NiTi with the solder. In this smart or adaptive reinforcement scheme, the reinforcements would first deform with the solder matrix in shear during thermomechanical loading of the solder joint, followed by snapping back to their original shape at the martensite-to-austenite ($M \rightarrow A$) transformation temperature, thus placing the solder in reverse shear. By imposing a back stress, the reverse shear would reduce the forward inelastic strains (plastic and creep) in the solder, thereby decreasing the overall inelastic shear-strain range to which the joint is subjected, leading to improvements in the TMF life of the solder. In addition, a fine dispersion of NiTi reinforcement particles in the solder would also help redistribute the large, local strain concentrations that induce failures in FC solder joints next to solder/bond pad interfaces⁴ and, thus, result in substantial potential improvements in joint life.

In this paper, we demonstrate the viability of this approach through thermomechanical-loading experiments on model single-fiber composite (SFC) solder joints. Furthermore, we report on our successful efforts at producing NiTi particulate-reinforced solder composites with a homogeneous reinforcement distribution, without using a coating on the NiTi particles.

EXPERIMENTAL

Thermomechanical Behavior

The TMC studies were conducted on monolithic solder joints, solder reinforced by $\text{Cu}/\text{Cu}_6\text{Sn}_5$ particulates, as well as a single martensitic NiTi fiber-reinforced solder composite. A 95.5Sn-3.8Ag-0.7Cu solder was used for all experiments.

The $\text{Cu}/\text{Cu}_6\text{Sn}_5$ -solder (C-S) composite was used to assess the impact of passive reinforcements and provide a baseline for comparison with NiTi-reinforced solders. The composite was fabricated by first mak-

* The Young's modulus (E) and flow stress (σ_f) of austenitic NiTi are around 83 GPa and 190 MPa, respectively, whereas those of solder are around 30 GPa and 30 MPa, respectively, at ambient temperature.^{21,22}

** For martensitic NiTi, E and σ_f are around 30 GPa and 50 MPa, respectively, in the annealed condition.^{21,22}

ing a thick paste of 5–10- μm -diameter, spheroidal Cu particles; sandwiching two layers of the paste between three solid solder disks; reflowing the sandwich in an aluminum crucible at 523 K under argon cover; and mechanically mixing the melt for 10 min. at 150 rpm using a stainless-steel, impeller-blade-type stirrer prior to solidification. The billet thus produced was rolled to a sheet from which 3-mm-diameter disks were punched out to prepare the joints for testing. The particulate volume fraction in this composite was about 0.7.

The NiTi-solder SFC was fabricated by casting the solder around a single 1-mm-diameter NiTi fiber ($\sim 50.6\%$ Ni), having an austenite start temperature, A_s , of ~ 310 K (Dynalloy Inc., Costa Mesa, CA). Prior to being placed in the graphite mold, the fiber was annealed at 823 K for 30 min to soften it. The surface of the fiber was ground with emery paper to remove native oxides and then covered with an HF-based commercial flux (Indalloy Flux #2, Indium Corporation of America, Utica, NY). The casting temperature was 533 K. Following solidification, approximately 3-mm-long pieces were cut from the SFC cylinder and used to produce the test joints. The fiber volume fraction of the SFC was 0.11.

Single-joint shear (SJS) specimens, comprising a single 2–3-mm-diameter solder joint between two 5-mm-diameter Cu rods, were then produced for the monolithic solder, the C-S composite, and the NiTi-solder SFC in two separate configurations. First, nominally 2-mm-diameter ball joints of the monolithic solder and the C-S composite were produced between the two copper rods, each of which had a raised bond pad of 1.6-mm diameter and 0.1-mm thickness at the joint end. All areas of the joint ends except the bond pads were coated with an Al thin film to serve as a solder mask to facilitate forming a ball shape during reflow. For these samples, the solder was reflowed for 2 min at 533 K while simultaneously adjusting the joint gap to produce nominally 1.2-mm-high, 2-mm-diameter, ball-shaped joints. The cooling rate following reflow was ~ 20 K/min. The SJS sample thus produced is depicted in Fig. 1 and represents a scaled up version of an FC or BGA joint used in microelectronic packages. Additional details of sample preparation are given in Ref. 4.

To evaluate the impact of the SMA reinforcement, SJS samples of the NiTi-solder SFC and monolithic solder were also produced with a cylindrical configuration. For these samples, the Cu rods had a circular recess of approximately 2-mm diameter and 0.2-mm depth at the joint ends to enable the fiber of the SFC to remain closely aligned with the axes of the Cu rods during reflow. The sample geometry is schematically depicted in Fig. 2, which also shows macrographs of the cylindrical SJS joints of the monolith and the SFC. These samples were reflowed for ~ 3 min at 533 K and cooled slowly to ambient temperature.

Following sample preparation, an instrumented, bimetallic load frame, using the thermal expansion mismatch between Al and Invar, was used to impart

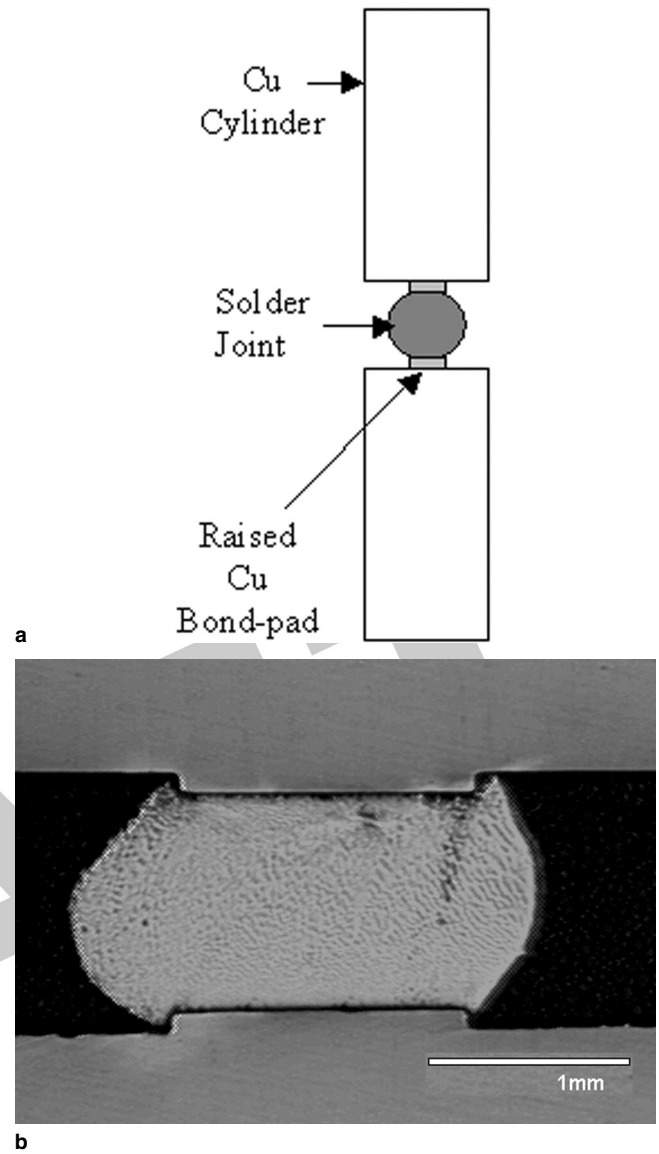


Fig. 1. (a) Schematic and (b) macrograph of the ball-shaped SJS sample used for TMC tests. The joint is attached to two copper cylinders at the two ends using raised circular pads.

temperature-dependent shear displacements to the joints in the SJS specimen. The instrument, described in detail in Ref. 4, uses several temperature-compensated strain gauges to produce continuous records of the applied force and shear displacement of the joint during thermal cycling. Each SJS specimen was subjected to 12 thermal cycles in argon from 298 K to 418 K with heating and cooling times of approximately 20 min each and dwell times of about 10 min at the maximum and minimum temperatures. The dimensions of the frame were such that the solder joint was subjected to a nominal shear strain range of ~ 0.03 in the experimental temperature range.

Processing of NiTi Particulate-Reinforced Solder

The 1-mm-diameter NiTi wires were first embrittled by cathodically charging with hydrogen using

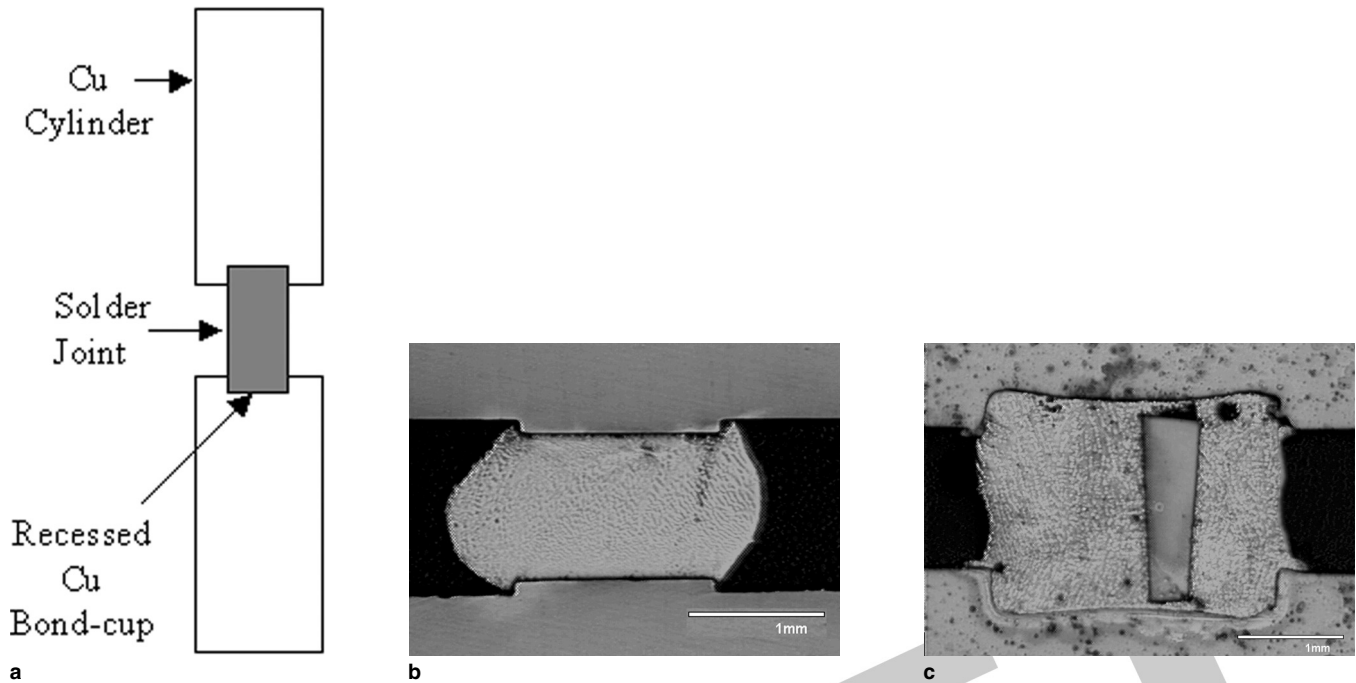


Fig. 2. (a) Schematic of the cylindrical SJS samples used for TMC tests on the monolithic solder and NiTi-solder SFC. The joint is attached to two copper cylinders at the two ends using recessed circular cups. Macrographs of the cylindrical SJS samples of (b) the monolithic solder and (c) the SFC.

a Pt anode and an electrolyte of 1-N H_2SO_4 with 0.2 g/L of thiourea. The embrittled wire was then ground to a powder using a mortar and pestle and sieved to yield particle sizes of $<15\text{ }\mu\text{m}$ by mechanical grinding in a mortar and pestle. Following grinding, the powder was heated in vacuum at 823 K for 1 h to drive off the dissolved hydrogen and anneal out the dislocation structure introduced during grinding. The powder was then mechanically mixed thoroughly with approximately 15 vol.% of a hydrofluoric acid-based flux (Indalloy flux #2, Indium Corporation of America) to produce a NiTi paste. The use of this flux ensured deoxidation of the powder particles and promoted wetting between NiTi and the solder during subsequent reflow.

Separately, a solder paste was produced using a solder powder of nominally 25- μm particle size and an adipic acid-based flux with polyethylene glycol and polypropylene glycol as the thixotropic agent and solvent, respectively,^{21,22} wherein the solder powder-to-flux ratio was about 7:1. The NiTi paste was then thoroughly mixed with the solder paste using an impeller-blade-type mechanical stirrer at 200 rpm, thus producing a NiTi particulate containing solder composite paste.

Finally, small quantities of the composite solder paste were dispensed with a syringe on an aluminum plate heated at 533 K, producing approximately 2-mm-diameter balls of the composite solder, as shown in Fig. 3. These balls were subsequently removed from the Al plate and prepared for metallographic and scanning electron microscopic examination.

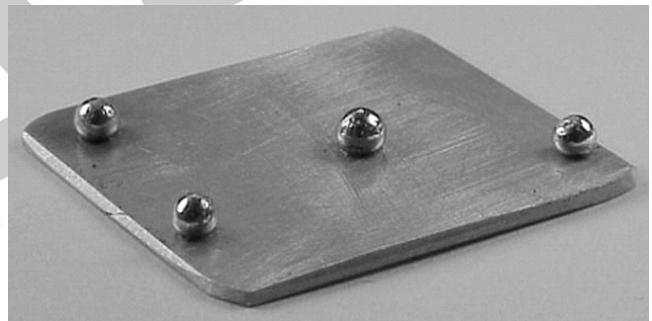


Fig. 3. NiTi particulate-reinforced solder, composite-solder balls of approximately 2-mm diameter on an aluminum substrate following surface cleaning.

RESULTS AND DISCUSSION

Thermomechanical Behavior

Microstructures

Figure 4 shows that the microstructure of the ball-shaped SJS joint of the monolithic solder consists of primary β -Sn grains surrounded by a divorced eutectic of fine Ag_3Sn (and some Cu_6Sn_5) particles in Sn. The primary grain size is $\sim 10\text{ }\mu\text{m}$, and the Ag_3Sn particle size is $\leq 0.5\text{ }\mu\text{m}$.

Figure 5a–c shows the microstructure of the SJS ball joint reinforced by 7vol.%Cu particles. The majority of the Cu particles reacted with the Sn matrix to form Cu_6Sn_5 intermetallics. This is shown in Fig. 5, where Cu_6Sn_5 is observed to form all around a Cu particle along the particle/matrix interface. Most of these particles were entrapped between the primary β -Sn grains during solidification (Fig. 5b) but were relatively uniformly

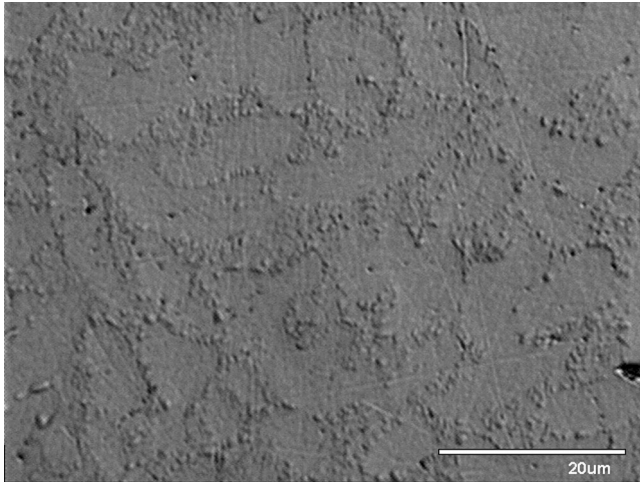


Fig. 4. Microstructure of the SJS joint of a monolithic solder, showing primary β grains surrounded by eutectic comprising intermetallic particles (Ag_3Sn , Cu_6Sn_5) in the Sn matrix.

distributed throughout the matrix, as shown in Fig. 5a. The microstructure of the composite matrix was close to that of the monolithic solder (Fig. 4). No evolution of the microstructure of either the matrix or the reinforcement was noted after the SJS sample was subjected to 12 cycles, suggesting that a comparison of the strain responses of the monolith and the composite would yield a direct assessment of the role of the $\text{Cu}/\text{Cu}_6\text{Sn}_5$ reinforcements.

Figure 6a and b shows the matrix and interfacial microstructures of a cylindrical SJS joint of the SFC. The matrix microstructure in Fig. 6a, which has a coarser eutectic than that found in ball joints, was very similar to that of the monolithic cylinders. No perceptible microstructural change was observed in either the SFC or the monolithic solder cylinder after 12 TMCs. Therefore, a comparison of the stress/strain records of the two samples is expected to provide direct insight into the role of the NiTi fiber

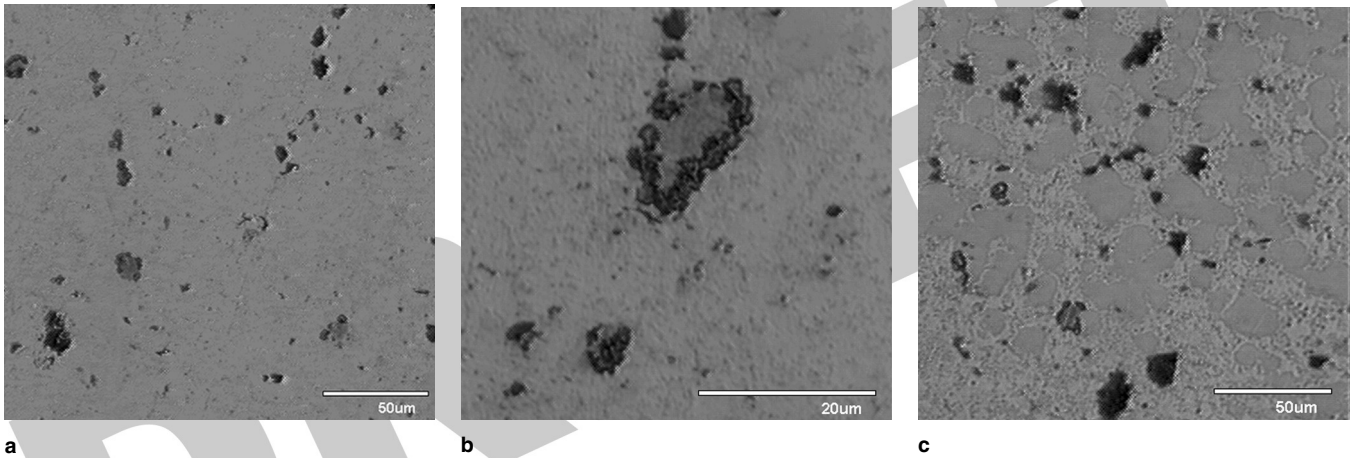


Fig. 5. Microstructure of the SJS ball joint of 7vol.%Cu particle-reinforced solder, showing (a) an even distribution of reinforcements, (b) Cu_6Sn_5 particles growing around a Cu particle, and (c) a micrograph revealing that the Cu_6Sn_5 particles are located between β primary grains.

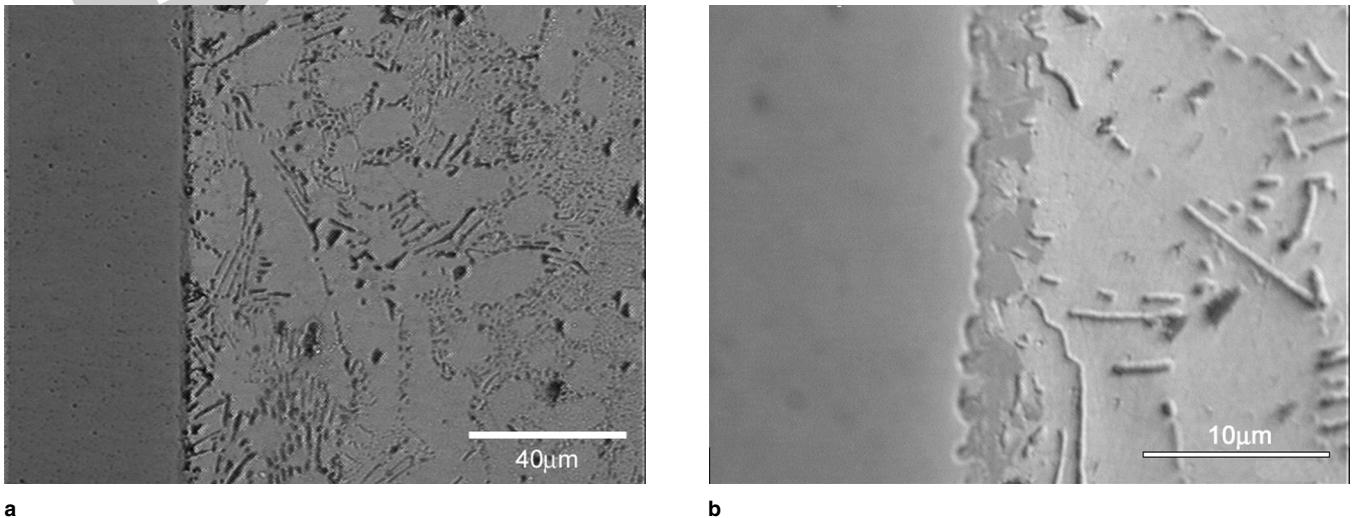


Fig. 6. Photographs revealing microstructures of the (a) matrix and (b) interfacial region of the NiTi-solder SFC. A distinct Ni_3Sn_4 layer is seen at the interface for a sample held at the reflow temperature (533 K) for about 10 min. The presence of this intermetallic layer suggests that the liquid solder wets the NiTi wire adequately following application of the flux.

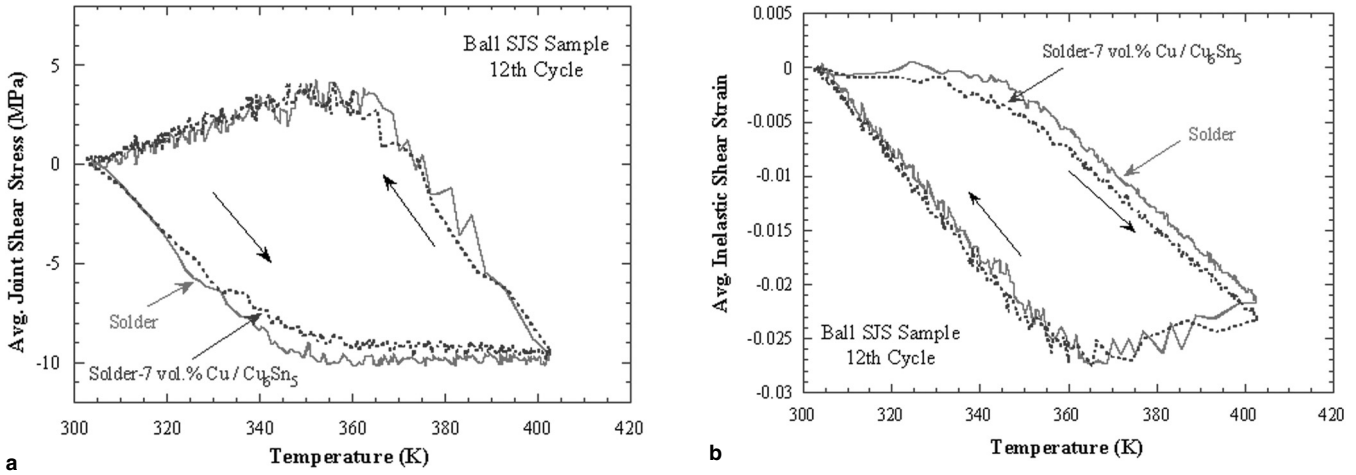


Fig. 7. Plots showing variation of the average shear stress and average inelastic-shear strain in ball-shaped SJS joints of the monolithic solder and Cu-solder composite during the twelfth TMC. The heating and cooling segments are indicated with arrows pointing toward the appropriate direction.

during TMC. Figure 6b shows a high magnification image of the interfacial region of an SFC sample that was held at the reflow temperature for 10 min. A thin layer of the Ni₃Sn₄ intermetallic is observed at the interface, suggesting that, during reflow, the wetting between the molten solder and NiTi at the interface was quite good following application of the flux.

Overall Behavior during TMC

Figure 7a shows an experimentally obtained plot of the average joint shear stress ($\bar{\tau}$)[†] versus temperature (T) during the twelfth TMC on the monolithic solder ball and the Cu-reinforced solder ball. Plots for the twelfth cycle are shown because it previously has been found to take several cycles (~3–5) for stable stress/strain hysteresis conditions to evolve.⁴ The experimental plots are qualitatively similar to those observed previously for Pb-Sn solders.⁴ Because the measurement starts with the joint in a stress-free state at ambient temperature (298 K), the joint stress initially builds up elastically (linearly) until local plasticity and creep mechanisms start operating. Beyond about 343 K, the plot shows nonlinearity with associated stress relief caused by creep. During cooling, stresses build up again, and below about 353 K, the joint is subject to significant inelastic strains with strain localization in shear bands, which allow the stress to return to a small value.

Importantly, it is observed from Fig. 7a that both the monolithic solder and the ball with 7vol.%Cu reinforcements show very similar behavior, with little discernible difference. This suggests that the passive reinforcements proffered by the Cu/Cu₆Sn₅ particulates have relatively little impact on the thermomechanical behavior of the solder, at least for volume percents of $\leq 7\%$. This is because the

compliant, creeping solder easily flows around the stiff reinforcements, which, because of their large spacing and small volume fraction, do not serve as significant obstacles to matrix flow.

Figure 7b shows a plot of the average inelastic-shear strain ($\bar{\gamma}_{inel}$)[‡] against temperature during the twelfth TMC. The observed inelastic-strain hysteresis is due to the operation of creep and plastic yielding. While heating from the ambient, no inelastic strain is induced initially as the joint is loaded elastically, following which high-temperature creep/plasticity mechanisms become operational. The inelastic strains increase rapidly, and during cooling, they steadily decrease to a near-zero value. As in Fig. 7a, little difference is noted in the inelastic-shear strain versus temperature behavior between the monolithic solder and the solder reinforced with Cu/Cu₆Sn₅ particles. This confirms that the passive Cu/Cu₆Sn₅ particulate reinforcements offer little dividend in terms of the thermomechanical behavior when present in small quantities ($\leq 7\%$).

Figure 8a plots $\bar{\tau}$ versus temperature during the twelfth cycle for the cylindrical samples of monolithic solder and the solder-11vol.%NiTi SFC. Some difference is noted between the two materials during heating, where the stress is observed to build up more rapidly in the NiTi fiber-reinforced composite. Correspondingly, as observed in Fig. 8b, which plots $\bar{\gamma}_{inel}$ versus T during the twelfth cycle for the monolith and the NiTi-solder SFC, $\bar{\gamma}_{inel}$ accrues much more slowly during heating in the SFC than in the monolith. This ultimately results in a significantly smaller inelastic-strain range, $\Delta\bar{\gamma}_{inel}$, in the SFC relative to the monolith, as noted from the smaller hysteresis for the SFC in Fig. 8b. Because the inelastic-strain range, $\Delta\bar{\gamma}_{inel}$, determines the LCF life of the joint, the reduction in $\Delta\bar{\gamma}_{inel}$ for the SFC is

[†] The average joint stress is computed by dividing the force by the average of the joint diameter at the middle and at the solder/bond pad interface. It should be noted that the local stresses in certain areas of the joint are significantly greater.⁴

[‡] $\bar{\gamma}_{inel}$ represents the average strain over the entire height of the joint. The local γ_{inel} values may be substantially greater than $\bar{\gamma}_{inel}$ in regions of strain localization.

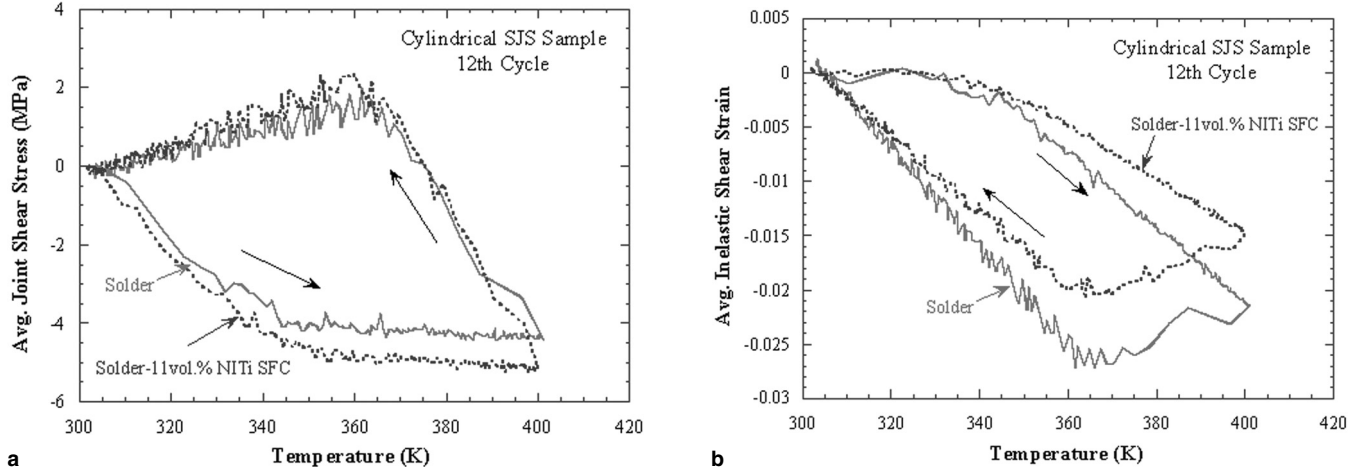


Fig. 8. Plots showing variation of the average shear stress and average inelastic-shear strain in cylindrical SJS joints of the monolithic solder and NiTi-solder SFC during the twelfth TMC. The heating and cooling segments are indicated with arrows pointing toward the appropriate direction.

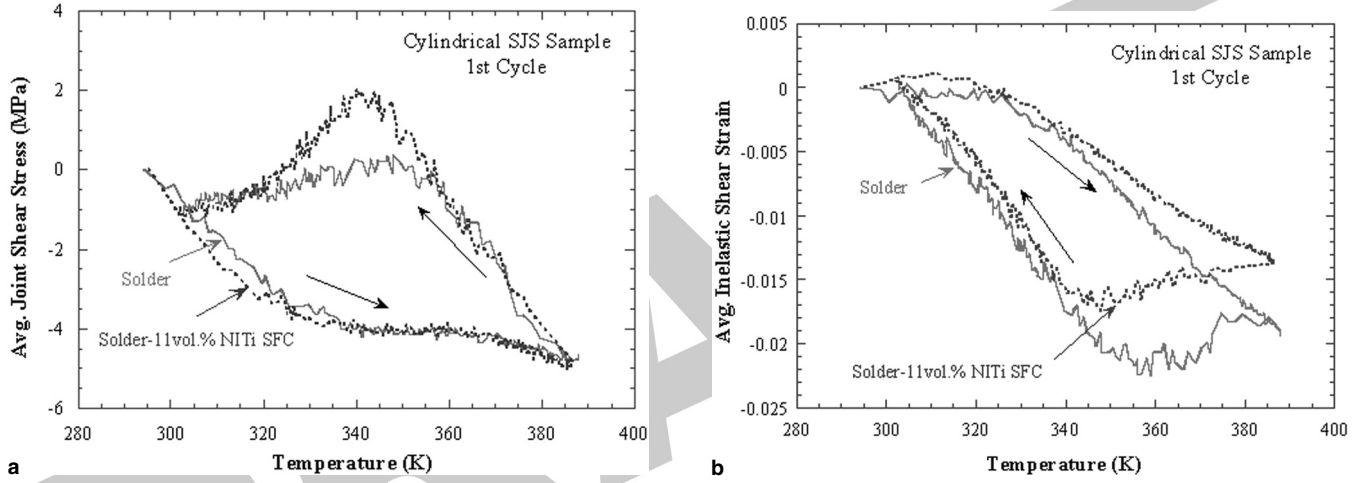


Fig. 9. Plots showing variation of the average shear stress and average inelastic-shear strain in cylindrical SJS joints of the monolithic solder and NiTi-solder SFC during the first TMC. The heating and cooling segments are indicated with arrows pointing toward the appropriate direction.

deemed to be of significant benefit in enhancing the LCF life of the SFC relative to the monolith.

Figure 9a and b shows plots of $\bar{\tau}$ versus T and $\bar{\gamma}_{inel}$ versus T , respectively, for the monolith and SFC during the first cycle. Although the basic trends are similar to those observed during the twelfth cycle in that the SFC displays a larger stress range and a commensurately smaller inelastic-strain range, the details are somewhat different. First, as in the twelfth cycle, it is noted that the inelastic strain accrues more slowly in the composite during heating, and this is directly responsible for the resulting smaller $\bar{\gamma}_{inel}$ range for the SFC. However, it is apparent that the comparative $\bar{\tau}$ versus T behavior of the SFC and monolith during the first cycle is quite different from that in the twelfth cycle. During cooling, the composite is stressed to a significantly higher level relative to the monolith prior to the onset of plastic-strain localization. This results in the prominent “knee” in the cooling part of the $\bar{\tau}$ versus T plot for the SFC in the first cycle, which is absent for the monolith. This suggests that during cooling in the first cycle, strain localization occurs in the monolith

much more easily (as indicated by the lower $\bar{\tau}$ level) than in the SFC.

An important point that emerges from Figs. 8 and 9 is that, although the maximum value of the inelastic-shear strain ($\bar{\gamma}_{inel,max}$) for the SFC is significantly smaller than that for the monolith in both cycles (by about 26%), the maximum $\bar{\tau}$ ($\bar{\tau}_{max}$) to which the joint is subjected is about 18% greater for the SFC in the twelfth cycle, whereas the difference is indiscernible for the first cycle. While it is expected that reinforcing the solder with stiff reinforcements would reduce $\bar{\gamma}_{inel,max}$, this would occur at the expense of an increased $\bar{\tau}_{max}$, as observed for the twelfth cycle. However, during the first cycle, a reduced $\bar{\gamma}_{inel,max}$ is noted for the SFC (relative to the monolith) without a commensurate increase in $\bar{\tau}_{max}$, suggesting that the fiber acts as more than just a passive reinforcement, as discussed later. This reduction of $\bar{\gamma}_{inel,max}$ without an associated increase in $\bar{\tau}_{max}$ is clearly beneficial from the point of view of an actual microelectronic application, where a significant reduction in the inelastic-strain range (with concomitant increase in LCF life) is desired, but without an increase in the

overall solder-stress level because a higher solder-stress level would subject the microelectronic device (i.e., the Si or GaAs chip) to greater stresses and, thus, enhance the likelihood of device failure.

Role of the Shape-Memory Effect of NiTi on TMC Response

From the preceding, it appears that reinforcement with martensitic NiTi does indeed yield the anticipated dividends, particularly during the first cycle, where the inelastic-strain range decreases significantly without increasing the maximum stress level. To understand the difference between the behaviors noted in the first and twelfth cycles, we now inspect the phase transition behavior of NiTi.

Figure 10 shows differential scanning calorimetry (DSC) scans of the NiTi wire during heating and cooling over two separate temperature ranges: (a) scan range 1: 238–353 K and (b) scan range 2: 283–348 K. In both experiments, the sample was equilibrated at the lowest temperature for 5 min prior to the scan. The sample was then heated to the maximum temperature at the rate of 10 K/min, where it was held for 5 min prior to being cooled at the same rate to the lowest temperature. For both scans, the sample weight was around 40 mg.

It is observed that when the scan is started after equilibration at 238 K, a single exothermic peak (peak A) occurs at 316 K. During equilibration at 238 K, the entire material is transformed to the martensitic B19' phase (trigonal structure). During heating, B19' transforms completely into the austenitic B2 (ordered bcc phase) at 316 K, and the material becomes single-phase austenitic above peak A. During subsequent cooling from 353 K, two distinct endothermic peaks are observed (B and C). Khalil-Allafi et al.²³ and Eggeler et al.²⁴ have demonstrated via a combination of transmission electron microscopy (TEM) and DSC that during this

two-stage transformation, the first peak (peak B at 295 K) is associated with the transformation of B2 into a mixture of the rhombohedral-martensitic phase R, which is the major constituent (~70 vol.%) and B19', which is the minor constituent. The second peak (peak C at 273 K) represents the transformation of the R phase to B19', thus producing a single-phase B19' structure. This kind of two-stage transformation occurs when Ni₄Ti₃ precipitates are present in the microstructure, and the precipitate/B2 interfaces promote the nucleation of the intermediate R phase during cooling. Because the present material was annealed at 823 K prior to the DSC experiments, a copious supply of Ni₄Ti₃ precipitates is expected in the microstructure, consistent with the two-stage transformation observed here.

A very different behavior is observed when the material is scanned starting from 283 K (scan range 2). As noted previously, at 283 K, a two-phase microstructure, consisting of R (major constituent) and B19' (minor constituent), is present along with Ni₄Ti₃ precipitates. During heating, the first peak (peak D at 301 K) corresponds to the transformation of R to B2, so that after this peak, the microstructure contains both B19' and B2. The B19' subsequently transforms to B2 at 316 K, corresponding to peak A. Because B19' constitutes only around 30 vol.% of the microstructure after peak D, the enthalpy change associated with peak A (i.e., the area under the peak) during the scan starting at 283 K is significantly smaller than that for the scan beginning at 238 K. On subsequent cooling to 283 K from 348 K, where a single-phase microstructure of B2 exists, only peak B corresponding to the B2 to B19' transformation is seen.

From the preceding discussion, it is clear that unless the NiTi is cooled below peak C (i.e., below ~263 K), a two-phase microstructure comprising R and B19' will exist at room temperature (291 K). Following casting of the solder-NiTi SFC and subsequent cooling, therefore, the NiTi wire reinforcement is expected to have a dual-phase martensitic R/B19' microstructure. Therefore, during the first TMC, which starts at ambient temperature, the M → A transformation is expected to occur over the range 296–323 K (corresponding to peaks D and A). At the end of each cycle, the temperature drops only to ~303 K (which is above both peaks B and C), and therefore, during subsequent cycles, no phase transformation would be expected in the present material. As a result, during subsequent cycles, the NiTi fiber would act as a passive reinforcement (with constant stiffness over the temperature range of the TMC), whereas, during the first cycle, the NiTi fiber would act as an adaptive or smart reinforcement. Therefore, the decrease in the inelastic-strain range and the corresponding increase in shear-stress range during the twelfth cycle are entirely caused by the presence of the stiff austenitic NiTi (B2) in the SFC. On the other hand, the decrease in inelastic-strain range without a commensurate

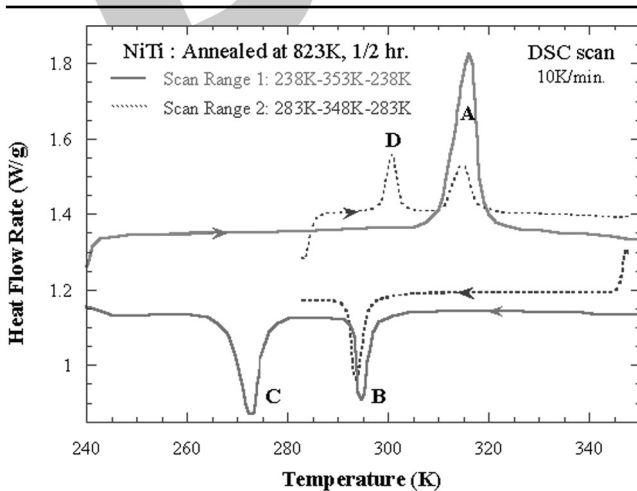


Fig. 10. DSC scans of the NiTi wire during heating and cooling over two separate temperature ranges: (a) 238–353 K and (b) 283–348 K. The endotherms A and D are associated with B19' → B2 and R → B2 transitions, respectively. The exotherms B and C are caused by B2 → R + B19' and R → B19', respectively.

increase in $\bar{\epsilon}_{\max}$ during the first cycle is associated with the $M \rightarrow A$ transformation during heating over the temperature range of 300–330 K.

From Fig. 10, it is clear that cooling the NiTi to ~ 260 K is essential for obtaining a completely B19' structure to derive the full benefit of the $M \rightarrow A$ (i.e., B19' \rightarrow B2) transformation during heating. Therefore, one of the cylindrical SJS joints was cooled to 253 K and held for 10 min after fabrication, thereby allowing the NiTi to transform completely to B19'. The joint was then subjected to three TMCs.

Figure 11 shows the initial part of the $\bar{\gamma}_{\text{inel}}$ versus T behavior (up to 363 K) during the heating segment of the first cycle for (1) the cylindrical, monolithic SJS joint; (2) the SFC sample cooled to ambient temperature after reflow; and (3) the sample cooled to 253 K prior to TMC. A trace for the heating segment of the twelfth cycle for the SFC is also shown. The approximate temperature range of the $M \rightarrow A$ transformation is marked by the arrows P and Q. For the monolith, $\bar{\gamma}_{\text{inel}}$ remains near zero for a while and then becomes increasingly negative. The same is true for the twelfth cycle of the SFC (which starts at 303 K), although here $\bar{\gamma}_{\text{inel}}$ is around zero over a larger temperature range (until ~ 328 K). In contrast, in both SFC samples, $\bar{\gamma}_{\text{inel}}$ initially increases with a positive magnitude, then decreases and becomes increasingly negative as the temperature increases.

In the monolith and the twelfth cycle of the SFC, $\bar{\gamma}_{\text{inel}}$ hovers around zero until the material starts deforming plastically and, then, moves in the same direction as the applied shear stress (i.e., negative). During the twelfth cycle of the SFC, initiation of inelasticity is delayed relative to the monolith (~ 328 K for the SFC and 310 K for the monolith) because the NiTi fiber in the SFC is in the stiff austenitic state right from the start. During the first cycle, on the

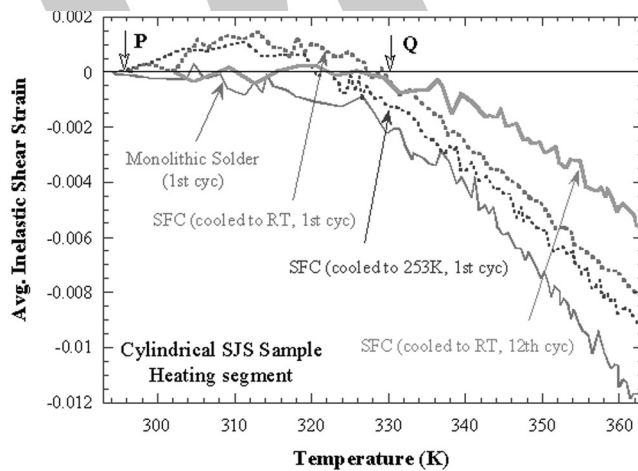


Fig. 11. Plot of the evolution of average inelastic-shear strain in cylindrical SJS joints of the monolithic solder and NiTi-solder SFC during the initial part of the heating segment of the first and twelfth TMCs. Whereas the inelastic strain is ~ 0 to slightly negative for the monolithic solder and the twelfth cycle on the SFC until ~ 330 K, the first cycle on the SFC shows a reverse (i.e., positive) inelastic strain during the $M \rightarrow A$ transformation range. When the SFC is cooled to 253 K prior to cycling, the magnitude of the reverse strain is larger.

other hand, we see evidence of reverse inelasticity (i.e., the direction of inelastic strain in the joint is opposite to the direction of applied stress) as the initially martensitic fiber undergoes transformation to austenite. As the solder joint is sheared in the negative direction during thermomechanical loading, the NiTi fiber also undergoes a negative strain. However, this is counteracted by a strain in the positive direction caused by the shape-memory effect. This positive strain places the solder matrix in the immediate vicinity of the NiTi wire in a positive shear-strain state, which is reflected in the plot (Fig. 11). Once the transformation is over (at 328 K), however, the composite deforms in the direction of the applied stress, and $\bar{\gamma}_{\text{inel}}$ becomes negative. This effect is more prominent in the sample cooled to 253 K after reflow (Fig. 11), where the extent of reverse strain during initial heating (over the transformation temperature range PQ) is found to be even greater, as would be expected because of the completely B19' microstructure and the commensurately greater extent of strain recovery expected during the B19' \rightarrow B2 transformation (as compared to the $R + B19' \rightarrow B2$ transformation in the sample cooled to room temperature).

This hypothesis is supported by Fig. 12, which shows DSC traces of the NiTi fiber after a 30-min anneal at 823 K, cooling to room temperature, followed by a reheat to 533 K, and subsequent cooling to 253 K. This heat-treatment sequence represented the conditions to which the NiTi fiber in the SFC SJS sample was exposed prior to the first cycle. The DSC scans are shown for three cycles corresponding to the TMC conditions of the SFC sample, where the heating segment of the first cycle starts at 253 K, but the cooling segment ends at 303 K. The second and third cycles each begin and end at 303 K. Under these conditions, a peak corresponding to the

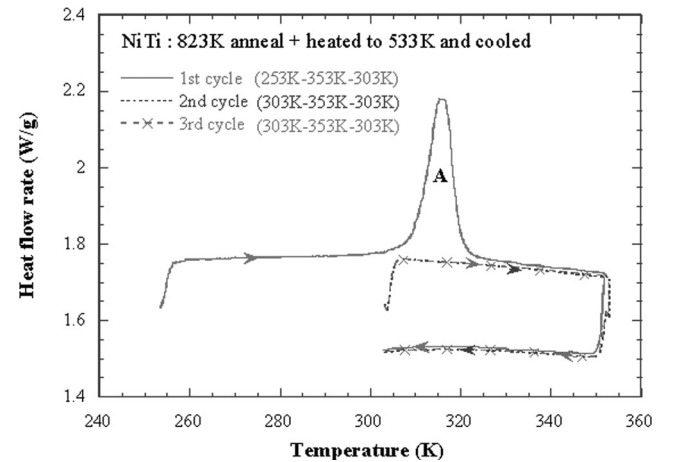


Fig. 12. DSC scan of the NiTi wire during three cycles simulating TMC conditions. Prior to scanning, the sample was annealed at 823 K for 30 min, cooled to ambient, heated to 533 K, and cooled to 253 K. The first heating segment shows only peak A (B19' \rightarrow B2). No peak is observed during the first cooling segment or during the second and third cycles, which begin at 303 K, thereby precluding the B2 to martensite transformation and, hence, the shape-memory effect.

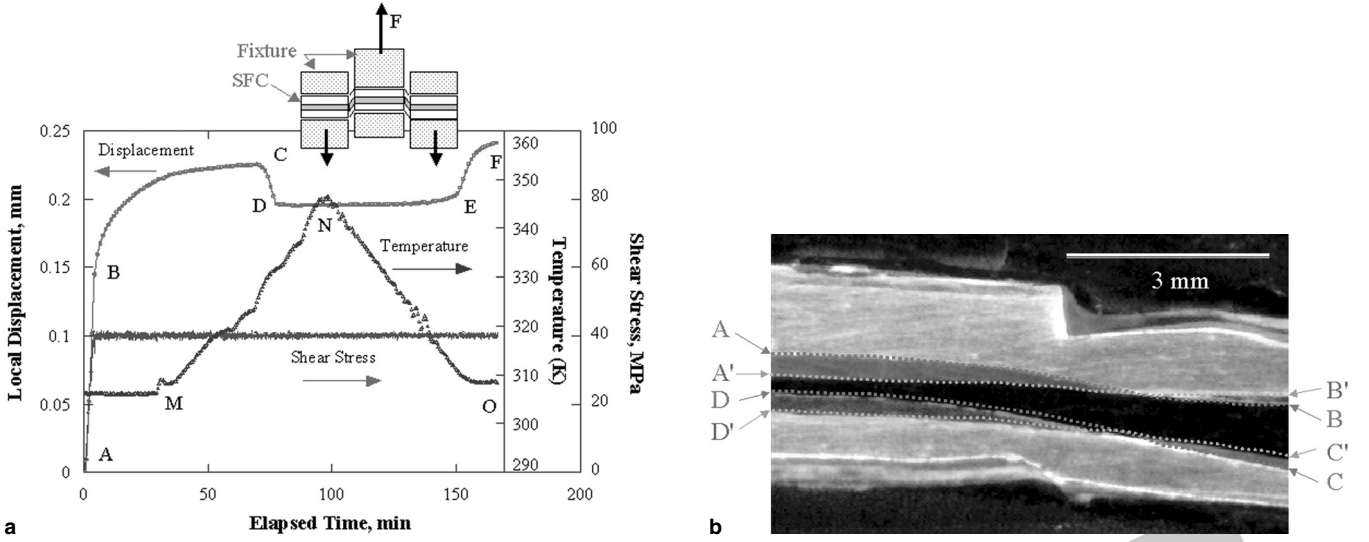


Fig. 13. (a) Shear displacement and temperature traces associated with the double shear test on the SFC, showing change in shear direction (segment CD) caused by $M \rightarrow A$ transformation at constant applied shear load. The inset shows loading geometry. (b) Superimposed macrographs of the shear-loaded SFC sample, showing NiTi fiber configurations after shear loading (ABCD) and after strain recovery caused by heating above the $M \rightarrow A$ transformation temperature ($A'B'C'D'$).

$B19' \rightarrow B2$ transformation with a large enthalpy change (which is proportional to the transformation volume) is noted between 305 K and 330 K during the first cycle. But no transformation is observed during the second and third cycles. Clearly, the shape-memory effect is only realized in the first cycle. Therefore, the NiTi fiber acts as an active or smart reinforcement only during the first cycle, being passive during subsequent cycles. This accounts for the reverse shear strain realized in the initial part of only the first cycle, as observed in Fig. 11 over the temperature range PQ, where the inelastic strain in the solder is positive even though the applied shear stress is negative.

Figure 13 provides direct evidence of the impact of $M \rightarrow A$ transformation in the fiber on the behavior of the SFC. As shown in Fig. 13a, the SFC was loaded in double shear to an average shear stress of 40 MPa at room temperature, which ensured plastic yielding of the NiTi wire at the center of the sample (point B). After this, the load was kept constant, but the material continued to deform via creep at room temperature. The data suggest a gradual decrease of the creep rate, likely associated with the transfer of the load from the solder to the NiTi wire. The temperature was then raised to 353 K and then decreased to ambient, as shown by the trace MNO in the figure. As observed in Fig. 13a, when the temperature reached ~ 320 K (point C), the measured shear displacement suddenly decreased from C to D (i.e., moved in a direction opposite to the applied shear force). This decrease in shear displacement in the segment CD is associated with the $M \rightarrow A$ transformation over the range 320–350 K. Because of the greater stiffness of austenite, the displacement remains relatively constant over the segment DE. Finally, once the temperature decreases to about 303 K, there is once again a displacement increase

of height EF (over 303–298 K), corresponding to the $A \rightarrow M$ transformation. Even though the $A \rightarrow M$ transformation did not occur during the cooling segment of the TMC experiments as noted earlier, this transformation is able to occur in the present constant-stress experiments possibly because the martensite start and finish temperatures (M_s and M_f) increase in the presence of applied stress.²² Figure 13b shows two superimposed macrographs of an SFC: (1) immediately after being loaded in shear and unloaded and (2) following heating to 353 K and cooling back to ambient temperature. After loading/unloading according to step (1), the sample was polished to reveal the fiber, photographed, and then heated/cooled as per step (2) and photographed again. In Fig. 13b, the perimeter of the longitudinal section of the NiTi fiber is shown as ABCD after the loading/unloading step and as $A'B'C'D'$ after the heating/cooling step.[#] Clearly, the shear strain accumulated in the NiTi during loading is largely recovered after heating to 353 K, as indicated by the observed straightening of the fiber, enabling loading of the SFC in reverse shear during heating. This experiment thus provides direct visual evidence that it is possible to obtain the desired reverse-shear deformation in the solder by first deforming the fiber along with the solder matrix and then obtaining shape recovery of the deformed fiber over the $M \rightarrow A$ transformation temperature range. This suggests that, at least in principle, NiTi reinforcements may be used to reduce the inelastic-strain range imposed on microelectronic solder joints.

It should be noted that because of the use of the NiTi reinforcement of $A_s \sim 310$ K in this work,

[#] In Fig. 13, the longitudinal section of the fiber appears tapered because the polishing plane was not perfectly parallel to the fiber axis.

the entire $M \rightarrow A$ transformation occurs by ~ 330 K (Fig. 12). During the first cycle of our experiments, TMC starts at 293 K. Therefore, only a small amount of inelastic strain ($<0.2\%$) is introduced into NiTi prior to complete transformation of the fiber to austenite. Hence, only a small strain recovery (i.e., reverse strain) was achieved in the present experiments, and the full potential of the shape-memory effect of the reinforcements was not realized. Future experiments are planned with NiTi having an A_s temperature of ~ 363 K, and this should allow loading of the fibers from 293 K to 363 K before the $M \rightarrow A$ transformation begins, thereby enabling a much larger strain recovery via the shape-memory effect.

Microstructure of the NiTi Particulate-Reinforced Solder Composite

In the following, we briefly discuss the microstructure of the 2-mm-diameter balls formed by reflowing the composite solder paste developed in our laboratory. Figure 14a shows the distribution of NiTi particles in the solder matrix, showing that the particulates have a nominally uniform distribution. The particulate volume fraction in the composite paste was approximately 0.1, and the particle size was determined to be 11.3 ± 4.83 μm . However, the final particulate volume fraction in the reflowed solder, as computed from the microstructure, was approximately 0.04, and the majority of the particulates observed in the microstructure were <5 μm in diameter (Fig. 14a). This is because during reflow, a significant proportion of the large NiTi particles is rejected as the approximately 25- μm solder particles in the composite paste melt and coalesce, leaving behind the larger particles in the boiling flux cover around the ball. This suggests that in order to increase the volume fraction of NiTi particles in the reflowed solder, the particle size needs to be reduced

to less than 5 μm . Figure 14b shows that the NiTi particles are mostly embedded in the eutectic micro-constituent between the primary β -Sn grains, indicating that the particles are pushed out as the primary phase forms and are entrapped in the last liquid to solidify (i.e., the eutectic). This is similar to the behavior noted for C-S composites, as shown in Fig. 5c. That the wetting of the NiTi by liquid solder is reasonably good is evidenced by the facts that (a) no large-scale clustering of particulates is noted, and (b) there are no noticeable voids between contiguous particles suggestive of surface tension-driven withdrawal of the melt from particulate interstices.

Figure 15 shows elemental x-ray maps from a region of the composite microstructure in the immediate vicinity of a NiTi particle. It is clear that the particle contains only Ni and Ti, whereas the matrix contains only Sn and Ag. No evidence of significant alloying of the liquid Sn with Ni is noted, at least for the reflow time of 2 min used to make this specimen, even though a reflow time of 10 min had yielded a distinct Ni_3Sn_4 interfacial layer in the SFC (Fig. 6b). The absence of a noticeable reaction layer is particularly clear by noting that the crack of submicron width in the lower part of the particle (indicated with an arrow in Fig. 5c) contains only Sn and Ag, with no indication of the presence of any dissolved Ni or Ti. Furthermore, the observation that the narrow crack is penetrated completely by the molten matrix also indicates that the wetting problem between NiTi and Sn, which has thwarted previous attempts at making NiTi-solder composites with an even particulate distribution,^{18–20} has been successfully overcome in this study. Finally, we note that the present work constitutes the first reported attempt at successfully making a NiTi-solder composite from a paste precursor, which is very important for the eventual application of these solder composites in commercial microelectronics.

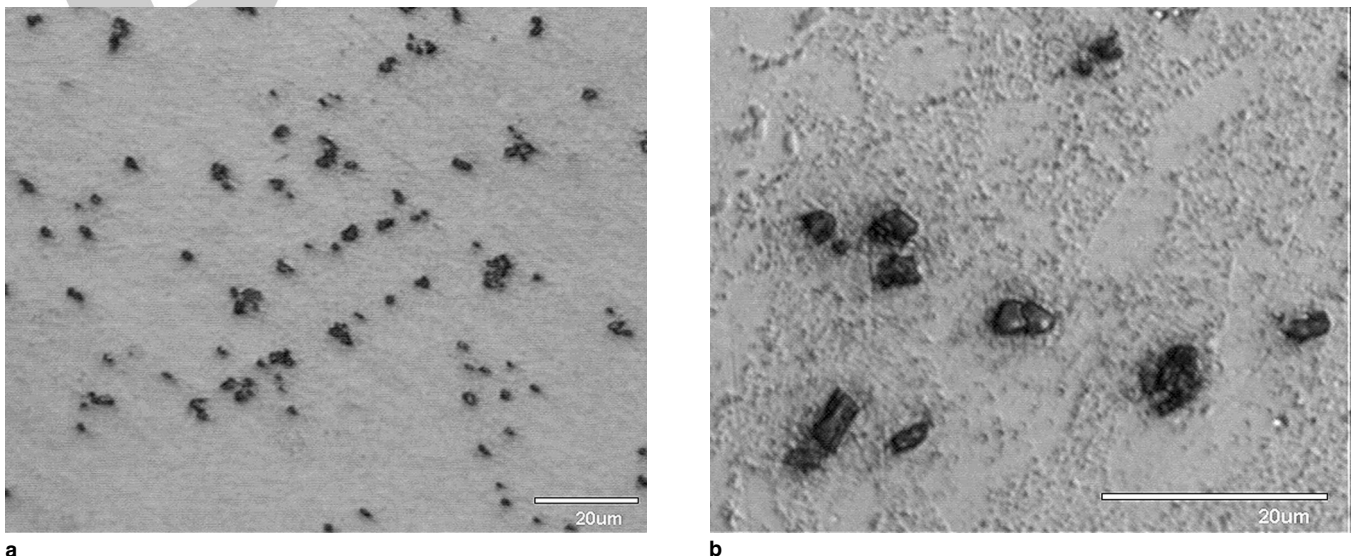


Fig. 14. Low and high magnification micrographs of a NiTi particle-reinforced adaptive SnAgCu solder ball (2-mm diameter) in the as-reflowed condition. The NiTi particles are distributed nominally uniformly throughout the ball.

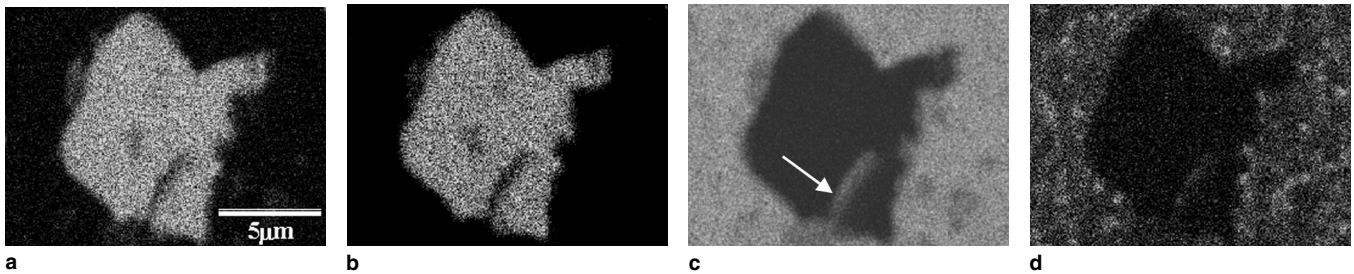


Fig. 15. Elemental x-ray maps of (a) Ni, (b) Ti, (c) Sn, and (d) Ag obtained from a region of the composite solder in the vicinity of a NiTi particle.

CONCLUSIONS

A new methodology to mitigate the effects of strain localization in microelectronic solder joints is proposed where the solder alloy is reinforced with reinforcements displaying the shape-memory effect. In this scheme, the SMA reinforcement is purported to deform in shear concurrently with the solder during TMC and, subsequently, undergo strain recovery through $M \rightarrow A$ transformation, thereby placing the solder matrix next to the reinforcements in reverse shear, potentially leading to reduced inelastic-strain localization within the solder and, therefore, enhanced joint life.

Thermal-mechanical loading experiments were conducted on a monolithic 95.5Sn-3.8Ag-0.7Cu solder, a Cu/Cu₆Sn₅ particle-reinforced solder, and NiTi-solder SFCs to elucidate the impact of the shape-memory effect on the overall joint behavior. It was found that the TMC behaviors of the monolithic solder and Cu/Cu₆Sn₅ particle-reinforced solder were very similar. On the other hand, the phase transformations occurring in NiTi were observed to reduce the inelastic-strain range to which a NiTi-solder SFC joint is subjected by ~25%, without enhancing the resultant stress range (i.e., without making the joint stiffer). The TMC experiments, in conjunction with DSC studies, clearly established that the $M \rightarrow A$ transformation occurring in the NiTi fiber during the heating segment imposes a shear strain opposite in sense to the applied shear stress on the solder joint. This was further demonstrated via double shear-loading experiments on the NiTi-solder SFC, where the direction of shear displacement was noted to become opposite the direction of applied shear over the $M \rightarrow A$ transformation temperature range. Visual evidence of shear-strain recovery of the SMA fiber in a SFC during heating after shear deformation is also presented, thereby validating the hypothesis that the NiTi acts as an active or smart reinforcement that enables the solder to react adaptively to external thermomechanical conditions.

Finally, the successful fabrication of a composite solder paste, from which adaptive solders with a uniform distribution of about 5 vol.% of NiTi particulates may be produced, has been presented. In this work, the acute wetting problem between NiTi and solder, which has thwarted previous attempts at making NiTi particulate-reinforced solder


composites, has been overcome, as evidenced by the microstructures presented.

ACKNOWLEDGEMENTS

This work was supported by the Army Research Office under Contract No. 42714MS, with Dr. David Stepp as the program monitor. The authors are grateful to Dr. Trelant Fang of FormFactor Inc., for his guidance and assistance in making the composite solder paste.

REFERENCES

1. H. Conrad, Z. Guo, Y. Fahmy, and D. Yang, *J. Electron. Mater.* 28, 1062 (1999).
2. P. Hacke, A.F. Sprecher, and H. Conrad, *J. Electron. Packaging* 115, 153 (1993).
3. P.L. Hacke, Y. Fahmy, and H. Conrad, *J. Electron. Mater.* 27, 941 (1998).
4. I. Dutta, A. Gopinath, and C. Marshall, *J. Electron. Mater.* 31, 253 (2002).
5. V. Sarihan, *Trans. ASME* 115, 16 (1993).
6. C.G. Kuo, S.M.L. Sastry, and K.L. Jerina, *Metall. Mater. Trans. A* 26A, 3265 (1995).
7. J.L. Marshall and J. Calderon, *Solder. Surf. Mount Technol.* 9, 22 (1997).
8. A.W. Gibson, K.N. Subramanian, and T.R. Bieler, *J. Adv. Mater.* 30, 19 (1998).
9. K.N. Subramanian, T.R. Bieler, and J.P. Lucas, *J. Electron. Mater.* 28, 1176 (1999).
10. J. Sigelko, S. Choi, K.N. Subramanian, J.P. Lucas, and T.R. Bieler, *J. Electron. Mater.* 28, 1184 (1999).
11. J.P. Lucas, F. Guo, J. McDougall, T.R. Bieler, K.N. Subramanian, and J.K. Park, *J. Electron. Mater.* 28, 1270 (1999).
12. J.H. Lee, D. Park, J.T. Moon, Y.H. Lee, D.H. Shin, and Y.S. Kim, *J. Electron. Mater.* 29, 1264 (2000).
13. S. Choi, J.P. Lucas, K.N. Subramanian, and T.R. Bieler, *J. Mater. Sci.* 11, 497 (2000).
14. J. McDougall, S. Choi, T.R. Bieler, K.N. Subramanian, and J.P. Lucas, *Mater. Sci. Eng. A* 285, 25 (2000).
15. C. Val, M. Leroy, and H. Boulharts, *Proc. 1993 Jpn. Int. Electronics Manufacturing Technology Symp.* 1993, pp. 50–53.
16. S. Trombert, J. Chazelas, P. Bonniay, W. Van Moorlegheem, M. Chandrasekharan, and J.F. Silvain, *Proc. 3rd ICIM/ECSSM* (1996), pp. 475–480.
17. S. Trombert, J. Chazelas, M. Lahaye, and J.F. Silvain, *Compos. Interfaces* 5, 479 (1998).
18. J.F. Silvain, J. Chazelas, M. Lahaye, and S. Trombert, *Mater. Sci. Eng. A* 273–275, 818 (1999).
19. J.F. Silvain, J. Chazelas, and S. Trombert, *Appl. Surf. Sci.* 153, 211 (2000).
20. O. Fouassier, S. Trombert, J.F. Silvain, J. Chazelas, D. Aslandis, A. Serneels, and W. Van Moorlegheem, *Proc. Shape-Memory Superelastic Technology* (1999), pp. 1–9.
21. ASM International, *Metals Handbook*, 10th ed. (Materials Park, OH: ASM International, 1990), vol. 2, pp. 897–902.
22. T.W. Duerig, *Engineering Aspects of Shape-Memory Alloys* (London: Butterworth-Heinemann, 1990).

- 
21. T. Fang, *Wiley Encyclopedia of Electrical and Electronics Engineering* (New York: John Wiley & Sons, Inc., 2002), vol. 7, p. 128.
 22. T. Fang, private communication.
 23. J. Khalil-Allafi, A. Dlouhy, and G. Eggeler, *Acta Mater.* 50, 4255 (2002).
 24. G. Eggeler, J. Khalil-Allafi, K. Neuking, and A. Dlouhy, *Z. Metallkd.* 93, 654 (2002).

DRAFT

Summary of Comments on JEM_997-R2

Page: 12

Sequence number: 1

Author: jdickey

Date: 3/3/2004 9:38:01 AM

Type: Note

Author: Reference 15: Is this entry okay as set?

Sequence number: 2

Author: jdickey

Date: 3/3/2004 9:45:43 AM

Type: Note

Author: Reference 16: Please provide publisher name and location.

Sequence number: 3

Author: jdickey

Date: 3/3/2004 9:39:27 AM

Type: Note

Author: Reference 20: Please provide publisher name and location.

Sequence number: 4

Author: jdickey

Date: 3/3/2004 9:54:57 AM

Type: Note

Author: Reference 22: Please provide opening and closing page numbers.

Sequence number: 5

Author: jdickey

Date: 3/3/2004 10:04:43 AM

Type: Note

Author: Reference 21 and 22: You have two references for 21 and two references for 22. Do you wish to renumber?
If so, they will need to be renumbered in the text as well.

Page: 13

Sequence number: 1

Author: jdickey

Date: 3/3/2004 9:54:13 AM

Type: Note

Author: Reference 21: Is Fang the editor? Is the closing page available?

Sequence number: 2

Author: jdickey

Date: 3/3/2004 9:56:20 AM

Type: Note

Author: Reference 22: Please provide the year.

Sequence number: 3

Author: jdickey

Date: 3/3/2004 10:04:13 AM

Type: Note

Author: Reference 21 and 22: You have two references for 21 and two references for 22. Do you wish to renumber?
If so, they will need to be renumbered in the text as well.

Online Proofing Guidance Page

FIRST STEP:

Install Adobe Acrobat Reader if you do not already have this or another Acrobat product installed on your computer. You can do this free of charge by connecting to the Adobe site and following the instructions at:

<http://www.adobe.com/products/acrobat/readermain.html>

SECOND STEP:

Please download and print your PDF file — we recommend that you save this file to disk, rather than opening it from within your Browser.

From a PC:

1. Right-click on the file/article link.
2. Select “Save Target as”
3. Select a desired location on your computer to save the file to, and click on “Save”
4. Open your PDF file directly with Acrobat Reader or another Acrobat product.
5. Print this file as you normally would with any typical application. Example: Go up to your toolbar, select “File”, select “Print”.

From a MAC:

1. Hold the mouse button down over the link.
 - a. In Internet Explorer, select “Download Link to Disk” from the resulting pop-up menu
 - b. In Netscape, select “Save this Link as” from the resulting pop-up menu
2. Select a desired location on your computer and click on “Save”
3. Open your PDF file directly with Acrobat Reader or another Acrobat product.
4. Print this file as you normally would with any typical application. Example: Go up to your menu bar, select “File”, select “Print”.

THIRD STEP:

Please go through the file you have just printed and thoroughly and clearly mark any revisions you would like to see implemented in your paper. If you have had any changes in phone/fax or e-mail addresses since your paper was submitted, please send us this new information.

FOURTH STEP:

Your revised paper needs to be faxed or mailed to:

IPC Print Services
Attn: Sheryl Dickenson
501 Colonial Drive
St. Joseph, MI 49085
Fax number: 1-269-983-4064

If you have questions regarding your paper in general, you may email or telephone:

IPC Print Services
Attn: Sheryl Dickenson
Email: sdickens@ipcjci.com
Phone: 1-269-983-7412, ext. 529